




Structure, Morphology, Cation Distribution and Magnetic Properties of Cr³⁺-Substituted CoFe₂O₄ Nanoparticles

Vishnu S. Shinde¹ · Vitthal Vinayak² · S. P. Jadhav¹ · N. D. Shinde¹ · Ashok V. Humbe³ · K. M. Jadhav³ 

Received: 30 April 2018 / Accepted: 14 June 2018 / Published online: 28 June 2018
© Springer Science+Business Media, LLC, part of Springer Nature 2018

Abstract

The present investigations deal with the effect of trivalent chromium ions (Cr³⁺) on structural and magnetic properties of nanocrystalline cobalt ferrite (CoFe₂O₄) nanoparticles. The samples of CoCr_xFe_{2-x}O₄ (where $x = 0.0$ to 1.0 in step of 0.2) were successfully synthesized by citric acid-assisted sol-gel auto combustion method. Further, the prepared samples were characterized by x-ray diffraction (XRD), scanning electron microscopy (SEM), infrared spectroscopy (IR) and pulsed field hysteresis loop technique for structural, morphological and magnetic properties analysis, respectively. XRD patterns showed the formation of single-phase cubic spinel structure with broad Bragg's peak for all the samples. The value of lattice parameter was found to be decreased with chromium substitution x . Cation distribution studies revealed that Co²⁺ and Fe³⁺ occupied both A and B sites, whereas Cr³⁺ ions occupied only B site. SEM analysis of the prepared samples confirmed the nanocrystalline nature of the material. The two absorption bands belonging to spinel structure were observed in IR spectra. Saturation magnetization (M_S), remanence magnetization (M_r) and coercivity (H_C) was found to be decreased with increase in chromium substitution x .

Keywords Cr³⁺ substitution · CoFe₂O₄ nanoparticles · XRD · Cation distribution · M - H curve

1 Introduction

Spinel ferrites basically recognized by the formula MFe_2O_4 (where M is divalent metal ion) have become the most requisite potential materials for technological perspective in a broad range of frequency ranging from microwave to radio frequency (RF) [1, 2]. The main advantage of spinel ferrite materials is the enormous compositional variability by the substitution of diverse cations in the parent crystal structure (i.e. at the tetrahedral and octahedral sublattices) and this disparity in cation distribution modifies many physical properties of spinel ferrites such as raise in DC resistivity, low dielectric losses and necessary magnetic character [3, 4].

Recently, investigations on nano-sized spinel ferrite particles have attracted substantial concentration for their various physical and chemical properties, which are strikingly different from those of their bulk counterpart [5]. Magnetic properties of spinel ferrite nanoparticles have been intensively studied and the mechanism of the size effect is generally well understood in terms of the magnetically inactive surface layer [6].

In case of mixed spinel ferrite nanoparticles, the magnetization and other magnetic properties are affected through the influence of small size [7]. The magnetic properties of the spinel ferrite materials originate from the anti-ferromagnetic coupling between two sublattices namely octahedral [B] and tetrahedral (A) sublattices. The net magnetization of spinel ferrite nanoparticles results from the difference between these two sublattices (A and B) [8].

In the family of spinel ferrites, cobalt spinel ferrites with cubic (FCC) structure possesses potential applications in the fields of high-density data storage [9], catalysis [10], medicine [11], sensors [12] and magnetic recordings [13]. Cobalt ferrites possessing partially inverse spinel structure (i.e. large portion of Co²⁺ occupies the octahedral B sites and the remaining small portion occupies the tetrahedral

✉ K. M. Jadhav
drjadhavkm@gmail.com

¹ Department of Chemistry, Shri Chhatrapati Shivaji College, Omerga, Osmanabad, India

² Department of Chemistry, B.S.S. College, Makni, Osmanabad, India

³ Department of Physics, Dr. Babasaheb Ambedkar Marathwada University, Aurangabad, Maharashtra, India

A sites) exhibits affirmative anisotropy constant [14], huge magnetostriction [15], high electrical resistivity [16] and good chemical stability [17].

The structural, microstructural, magnetic and electric properties of spinel cobalt ferrite nanoparticles depend upon numerous factors including the way of synthesis, composition of constituents, structure or size and the quantity and type of the substituent [18, 19]. Discrepancy of the cation distribution over A and B sites in the cobalt spinel lattice leads to modified magnetic and electric properties [20]. Many times, the alteration of Fe^{3+} ions with trivalent cations such as Al^{3+} , Nd^{3+} , Gd^{3+} , Ho^{3+} , La^{3+} , and Cr^{3+} in spinel cobalt ferrite is essential to attain definite objectives such as increase of DC resistivity, lowering of saturation magnetization and the high-temperature applications [21–23]. Spinel cobalt ferrites having two different cation sites offers the prospective for influencing its DC electrical as well as magnetostrictive properties by tailoring the site occupancy preference ability of the cations. This motivated us to carry out the work on trivalent ion-substituted spinel cobalt ferrite nanoparticles in a systematic manner. The trivalent ions substitution in B site of spinel cobalt ferrite and its effect on the magnetic and electrical properties was studied by many authors [24–28]. But there are only few reports available on structural, morphological, cation distribution and magnetic properties of sol-gel-synthesized Cr^{3+} -substituted spinel cobalt ferrite nanoparticles [29, 30].

Thus, herein, we report sol-gel auto combustion synthesis of trivalent Cr^{3+} -substituted CoFe_2O_4 nanoparticles with generic formula $\text{CoCr}_x\text{Fe}_{2-x}\text{O}_4$ (where $x = 0.0$ to 1.0 in the step of 0.2). Further, the effect of trivalent Cr^{3+} ions on structural, morphological, cation distribution and magnetic properties of CoFe_2O_4 nanoparticles were reported.

2 Experimental

2.1 Synthesis Procedure

The A.R. grade citric acid ($\text{C}_6\text{H}_8\text{O}_7 \cdot \text{H}_2\text{O}$), ferric nitrate ($\text{Fe}(\text{NO}_3)_3 \cdot 9\text{H}_2\text{O}$), cobalt nitrate ($\text{Co}(\text{NO}_3)_2 \cdot 6\text{H}_2\text{O}$) and chromium nitrate ($\text{Cr}(\text{NO}_3)_3 \cdot 4\text{H}_2\text{O}$) (>99%) were used as starting materials. The dextrose was used as a fuel. The dextrose to nitrate ratio was considered to be 4:1. The metal nitrates were dissolved together in a minimum amount of deionized water to get a clear solution. An aqueous solution of dextrose was mixed with metal nitrates solution. Then, ammonia solution was slowly added to adjust the pH at 8. The mixed solution was moved on a hot plate with continuous stirring around 80°C . During evaporation, the solution becomes viscous and finally forms a very viscous brown gel. When finally, all remaining water was released from the mixture, the sticky mass began to bubble. After

several minutes, the gel automatically ignited and burnt with glowing flints. The decomposition reaction would not stop before the whole citrate complex was consumed. The auto ignition was completed within a minute, yielding the brown-coloured ashes termed as per precursor. Further, the samples were fired at 600°C for 6 h for better crystallinity.

2.2 Characterizations

Roomtemperature x-ray diffraction patterns were recorded using Philips x-ray diffractometer (model 3710, at TIFR Mumbai). XRD patterns were recorded in the 2θ range of 20° to 80° using $\text{Cu-K}\alpha$ radiation. X-ray density (d_x) was evaluated by the mass/volume relation method. The experimental density (d_{exp}) was found using Archimedes's principal, in which the specimen was weighed in air and in xylene at room temperature, $\rho_{\text{exp}} = \text{weight of the sample in air/loss of weight in xylene}$. The SEM micrographs of typical samples were recorded using (JEOL-JS-M840 at T.I.F.R. Mumbai) scanning electron microscope. The IR spectra were recorded for all the samples with the help of PerkinElmer spectrometer (Model 783) in the frequency range of 300 to 800 cm^{-1} . The magnetic properties like (M_s), magneton number (n_B), and coercivity (H_C) are measured using pulse field hysteresis loop technique. The magnetization measurements were carried out in the field of 0.5 Tesla at room temperature.

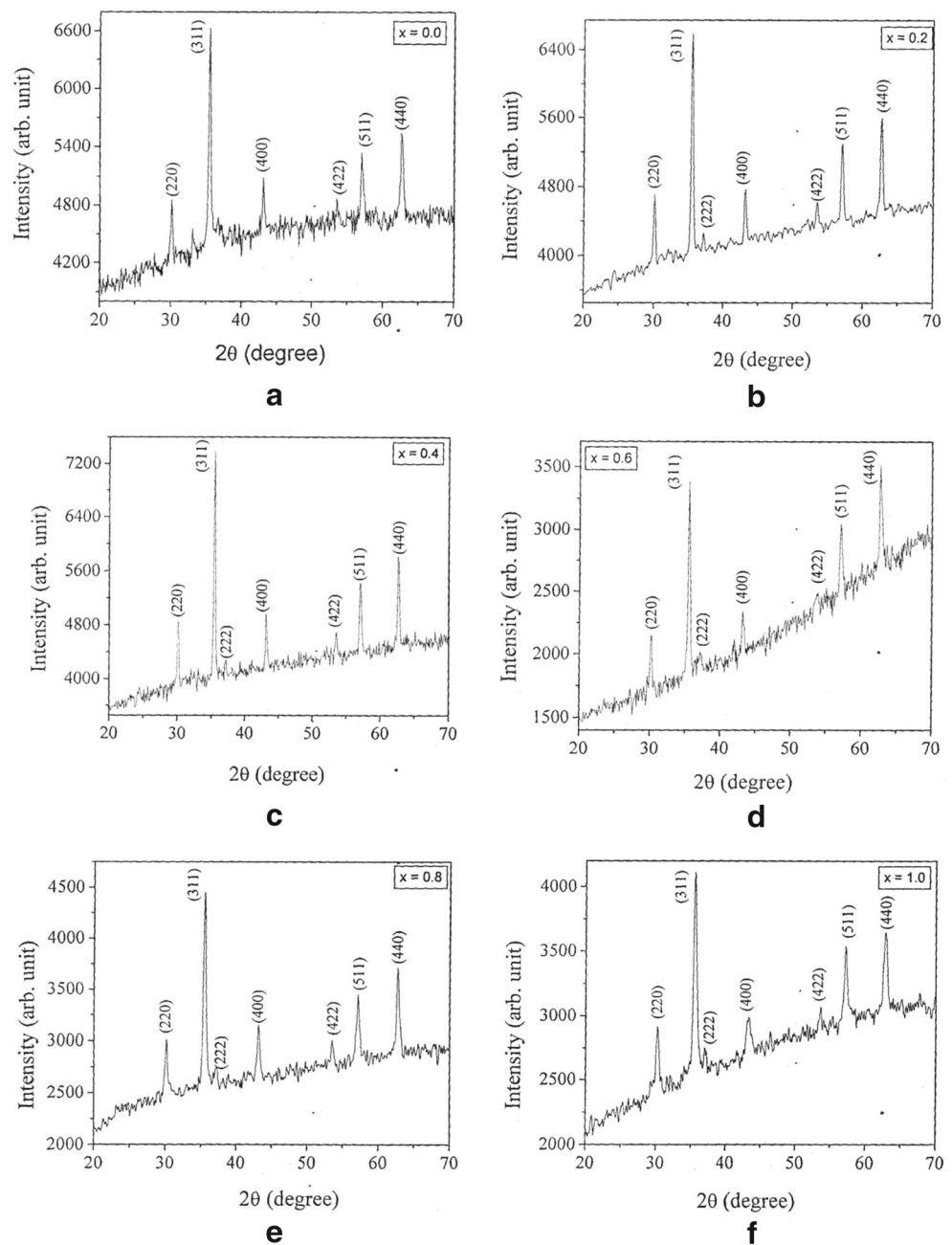
3 Results and Discussion

3.1 X-ray Diffraction Analysis

The x-ray diffraction patterns of $\text{CoCr}_x\text{Fe}_{2-x}\text{O}_4$ (where $x = 0.0$ to 1.0 in step of 0.2) nanoparticles are shown in Fig. 1a–f. The diffraction patterns and data indicate that all the samples possess cubic spinel structure. The x-ray diffraction pattern shows the reflection namely (220), (311), (222), (422), (400) and (511) which belongs to cubic spinel structure. The Bragg's peaks in the XRD pattern are slightly broader indicating the nano-sized nature of the samples. The most intense peak (311) of the XRD pattern has been considered to determine the particle size of the samples. Scherrer's formula was used to obtain particle size and the values of the particle size for all the compositions are listed in Table 1. It can be seen from Table 1 that the particle size varies from 26 to 38 nm. The XRD data was also used to evaluate cell dimensions (lattice constant a). The values of lattice constant were also given in Table 1.

The variation of lattice constant is shown in Fig. 2. It is observed that lattice constant decreases linearly with the substitution of chromium ions and obeys Vegard's law [31]. The decrease in lattice constant in the present study

Fig. 1 a–f XRD patterns of $\text{CoCr}_x\text{Fe}_{2-x}\text{O}_4$ spinel ferrite nanoparticles (for $x = 0.0$ to 1.0 in step of 0.2)



is attributed to the difference in ionic radii of Fe^{3+} and substituent Cr^{3+} . Usually, when ions of larger ionic radii are replaced by the smaller ionic radii in the spinel lattice, the decrease in lattice constant is observed. In the present case Fe^{3+} ions of larger radii (0.67 Å) are replaced by Cr^{3+} ion of smaller ionic radii (0.63 Å) and hence we observed the decrease of the lattice constant with increase in chromium substitution. Similar trend of lattice constant was also reported in chromium substituted cobalt ferrite system [32, 33].

The unit cell volume was also calculated using the values of lattice constant and are listed in Table 1. It is observed

that volume of the unit cell decreases with increase in chromium substitution. The x-ray density (d_x) of all the samples was also calculated from XRD data. The values of x-ray density are given in Table 1 and variation is shown in Fig. 3. X-ray density increases with increase in chromium substitution. The x-ray density is in the range of 5.298–5.379 g/cm^3 . The bulk density of the specimen has been determined accurately by the hydrostatic method.

The values of bulk density are presented in Table 1. The porosity of the samples was calculated using the value of x-ray and bulk densities and are reported in Table 1. The surface area was determined by using the following relation

Table 1 Values of lattice constant (a), crystallite size (t), unit cell volume (V), x-ray density (d_X), bulk density (d_B), porosity particles (P), grain size (G) and specific area (S) of $\text{CoCr}_x\text{Fe}_{2-x}\text{O}_4$ spinel ferrite nanoparticles

Structural parameters	Composition x						
	0.0	0.2	0.4	0.6	0.8	1.0	
a (Å)	8.379	8.361	8.351	8.331	8.316	8.291	
t (nm)	38	35	34	31	27	26	
V (Å ³)	588.3	584.5	582.4	578.2	575.1	569.9	
d_X (g/cm ³)	5.298	5.315	5.316	5.337	5.348	5.379	
d_B (g/cm ³)	4.550	4.610	4.680	4.730	4.760	4.830	
P (%)	14.12	13.26	11.96	11.37	10.99	10.21	
G (nm)	–	32	–	30	–	–	
S (m ² /g)	43.04	39.51	38.37	34.85	30.29	29.00	

$S = 6000/\rho d$, where, ρ is x-ray density, d is average particle size and S is surface area. The values of surface area are included in Table 1. It can be observed from Table 1 that all the samples show large surface area and vary with the chromium substitution.

The distance between magnetic ions (hopping length) at tetrahedral A sites and octahedral B sites was calculated for all the samples using the standard relation [34]. The values of hopping length L_A and L_B are given in Table 2. Figure 4 gives the variation of hopping length with the composition x .

It can be seen from Fig. 4 that both L_A and L_B decreases with chromium content x . The observed behaviour of hopping length with chromium content x is attributed to decrease in the lattice parameter. The bond length of tetrahedral A site d_{AX} and octahedral B site d_{BX} , tetrahedral edge d_{AXE} , shared octahedral edge d_{BXE} and unshared octahedral edge d_{BXEU} are calculated by using the experimental values of lattice parameter a and oxygen positional parameter u .

The values of allied parameters calculated from above mentioned expression are presented in Table 2. The Table 2 indicates that the tetrahedral bond length d_{AX} and octahedral bond length d_{BX} decreases as Cr^{3+} content x increases. Table 2 shows that the tetrahedral edge d_{AXE} , unshared octahedral edge d_{BXEU} does not vary much with composition while shared octahedral edge d_{BXE} decreases. This could be related to the smaller radius of Cr^{3+} ions as compared to Fe^{3+} ions and the fact that Cr^{3+} occupies strongly tetrahedral B site.

3.2 SEM Analysis

Scanning electron micrographs (SEM) of the typical samples $x = 0.4$ and $x = 0.6$ is shown in Fig. 5. It can be observed from the SEM images that the prepared samples are amorphous and porous in nature. Particle size obtained by SEM intersect method is of the nanometer dimension and the values are given in Table 1.

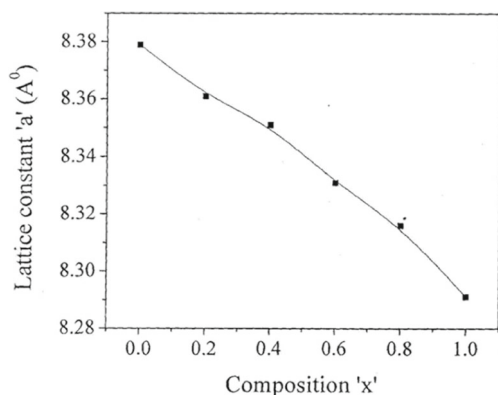
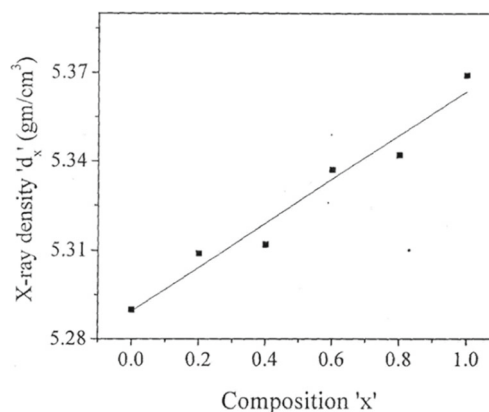
**Fig. 2** Variation of lattice constant a with composition x of $\text{CoCr}_x\text{Fe}_{2-x}\text{O}_4$ spinel ferrite nanoparticles (for $x = 0.0$ to 1.0 in step of 0.2)**Fig. 3** Variation of x-ray density (d_X) with composition x of $\text{CoCr}_x\text{Fe}_{2-x}\text{O}_4$ spinel ferrite nanoparticles (for $x = 0.0$ to 1.0 in step of 0.2)

Table 2 Values of hopping length of tetrahedral site (L_A), octahedral site (L_B), ionic radii (r_A and r_B), oxygen parameter (u), theoretical lattice constant (a_{th}) tetrahedral bond (d_{AX}), octahedral bond (d_{BX}), tetra edge (d_{AXE}), and octa edge (d_{BXE}) of $CoCr_xFe_{2-x}O_4$ spinel ferrite nanoparticles

Structural parameters	Composition x					
	0.0	0.2	0.4	0.6	0.8	1.0
L_A (Å)	3.628	3.620	3.616	3.607	3.601	3.590
L_B (Å)	2.962	2.956	2.953	2.945	2.940	2.931
r_A (Å)	0.683	0.682	0.680	0.679	0.678	0.677
r_B (Å)	0.689	0.722	0.756	0.790	0.823	0.857
u (Å)	0.3880	0.3882	0.3883	0.3885	0.3887	0.3891
a_{th} (Å)	8.381	8.368	8.359	8.333	8.320	8.297
d_{AX} (Å)	1.901	1.897	1.895	1.890	1.887	1.881
d_{BX} (Å)	2.048	2.043	2.041	2.036	2.032	2.026
d_{AXE} (Å)	3.104	3.097	3.094	3.086	3.081	3.072
d_{BXE} (Å)	Shared	2.820	2.814	2.810	2.804	2.799
	Unshared	2.970	2.964	2.960	2.953	2.948

3.3 Cation Distribution

The cation distribution in the spinel ferrite system $CoCr_xFe_{2-x}O_4$ was determined by x-ray intensity ratio calculation method. The details of the method used for the determination of cation distribution were already explained in our previous reports [35]. Similar procedure was adopted in the present study. The results of cation distribution are illustrated in Table 3. It is evident from Table 3 that chromium ions totally occupy octahedral B site, whereas, Co^{2+} and Fe^{3+} ions are partially occupied at tetrahedral A and octahedral B site. The Fe_A/Fe_B ratio increases with chromium substitution which leads to decrease in magnetization. The variation of iron ratio at B and A sites as a function of composition x is depicted in Fig. 6. Cr^{3+} ions occupy octahedral B site by replacing Fe^{3+} ions. The

observed and calculated intensity ratios (Table 3) are in close agreement with each other which suggest that the estimated cation distribution is correct. The mean ionic radius of the tetrahedral A and octahedral B site (r_A and r_B) can be calculated by the standard relations [36]. The values of r_A and r_B are given in Table 3. It is clear that both r_A and r_B decreases with increase in Cr content x . The decrease in r_A and r_B is due to the replacement of Fe^{3+} ions (0.67 Å) by smaller Cr^{3+} ions (0.63 Å) at both sites. The variation of r_A and r_B and oxygen parameter u and variation of ionic radii (r_A and r_B) with x is given in Fig. 6.

The theoretical values of lattice parameter were calculated using the standard equation and the values of theoretical lattice parameter a_{th} are given in Table 3. The theoretical lattice parameter decreases with increase in Cr content x . The variation of theoretical values is similar to that observed for experimentally determined lattice constant.

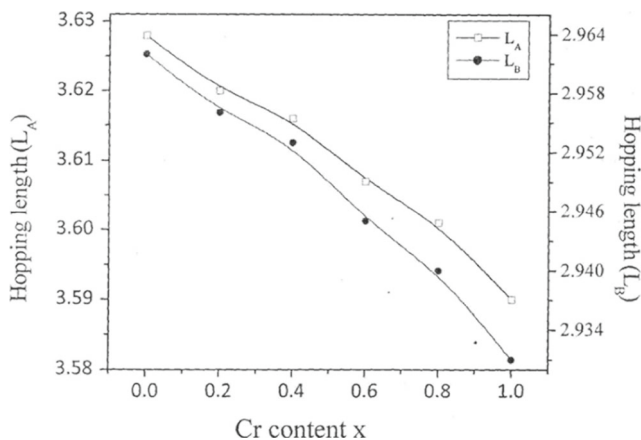


Fig. 4 Variation of hopping lengths (L_A and L_B) with composition x of $CoCr_xFe_{2-x}O_4$ spinel ferrite nanoparticles (for $x = 0.0$ to 1.0 in step of 0.2)

3.4 Infrared Spectroscopy Analysis

Figure 7a–f depicts the IR spectra for $CoCr_xFe_{2-x}O_4$ spinel ferrite system under investigation. Two prominent absorption bands are seen in the IR spectra which looks different than the IR spectra of bulk samples. The two major absorption bands are found to be broad, which is attributed to smaller particle dimensions of the samples.

The two absorption bands are assigned to intrinsic vibrations of molecules at tetrahedral A and octahedral B sites and are denoted by ν_1 and ν_2 respectively. The values of ν_1 and ν_2 are given in Table 4. These values are in reported range and are used to determine force constant K_t and K_o [37]. The values of force constant are given in Table 4. It can be seen from the table that K_t and K_o

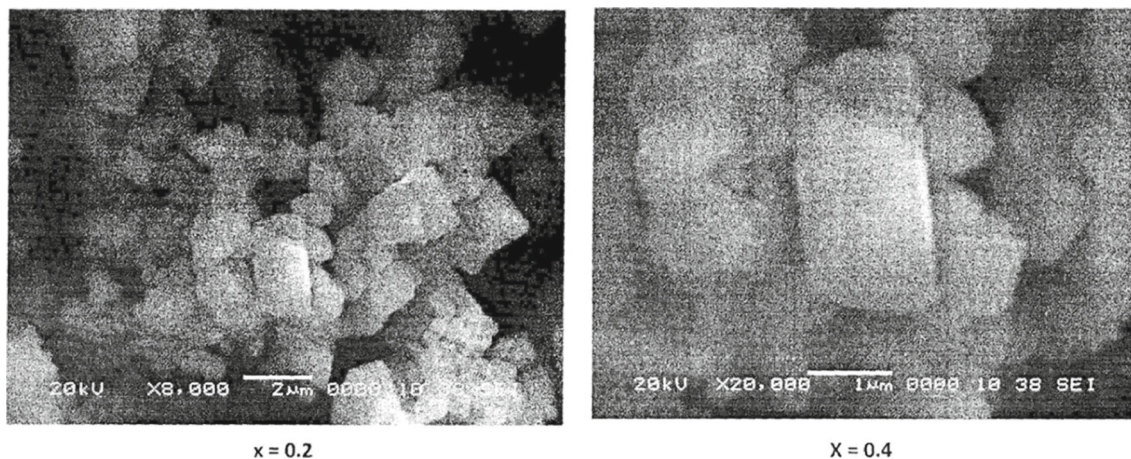


Fig. 5 SEM images of $\text{CoCr}_x\text{Fe}_{2-x}\text{O}_4$ spinel ferrite nanoparticles (for $x = 0.2$ and 0.6)

Table 3 Cation distribution, observed and calculated intensity ratios of $\text{CoCr}_x\text{Fe}_{2-x}\text{O}_4$ spinel ferrite nanoparticles

Com. x	Cation distribution		$\lambda(\text{Fe}^{3+})_{\text{B}}/[\text{Fe}]^{3+}$	$I(400)/I(440)$		$ I(220)/I(440) $	
	A site	B site		Obs.	Cal.	Obs.	Cal.
0.0	$\text{Co}_{0.26}\text{Fe}_{0.78}$	$\text{Co}_{0.74}\text{Fe}_{1.26}$	0.587	0.936	1.103	1.360	1.121
0.2	$\text{Co}_{0.24}\text{Fe}_{0.76}$	$\text{Co}_{0.76}\text{Cr}_{0.2}\text{Fe}_{1.04}$	0.731	0.869	0.611	0.657	0.548
0.4	$\text{Co}_{0.20}\text{Fe}_{0.80}$	$\text{Co}_{0.80}\text{Cr}_{0.4}\text{Fe}_{0.80}$	1.000	1.111	1.127	1.098	1.002
0.6	$\text{Co}_{0.18}\text{Fe}_{0.82}$	$\text{Co}_{0.82}\text{Cr}_{0.6}\text{Fe}_{0.58}$	1.414	0.990	0.829	1.000	0.847
0.8	$\text{Co}_{0.15}\text{Fe}_{0.85}$	$\text{Co}_{0.85}\text{Cr}_{0.8}\text{Fe}_{0.35}$	2.429	1.097	1.044	1.062	1.031
1.0	$\text{Co}_{0.14}\text{Fe}_{0.86}$	$\text{Co}_{0.86}\text{Cr}_{1.0}\text{Fe}_{0.14}$	6.143	0.947	0.494	1.028	0.499

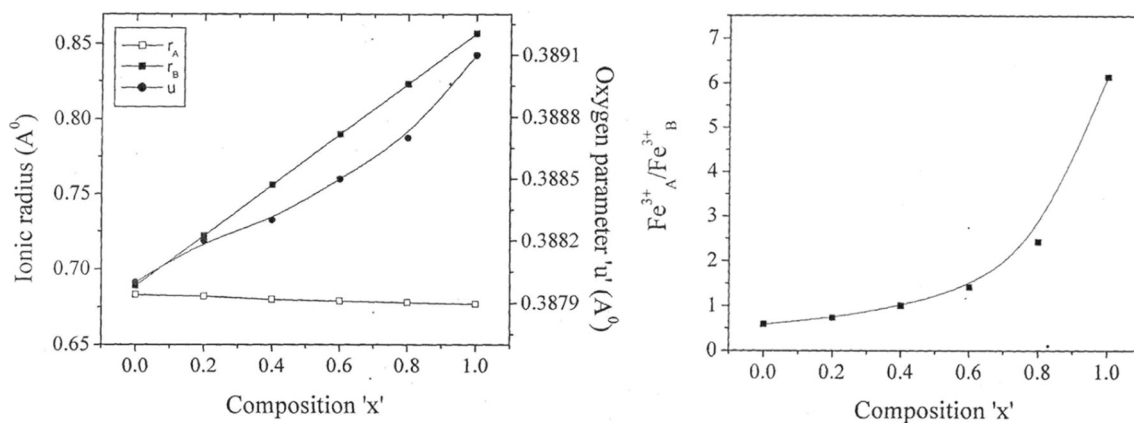
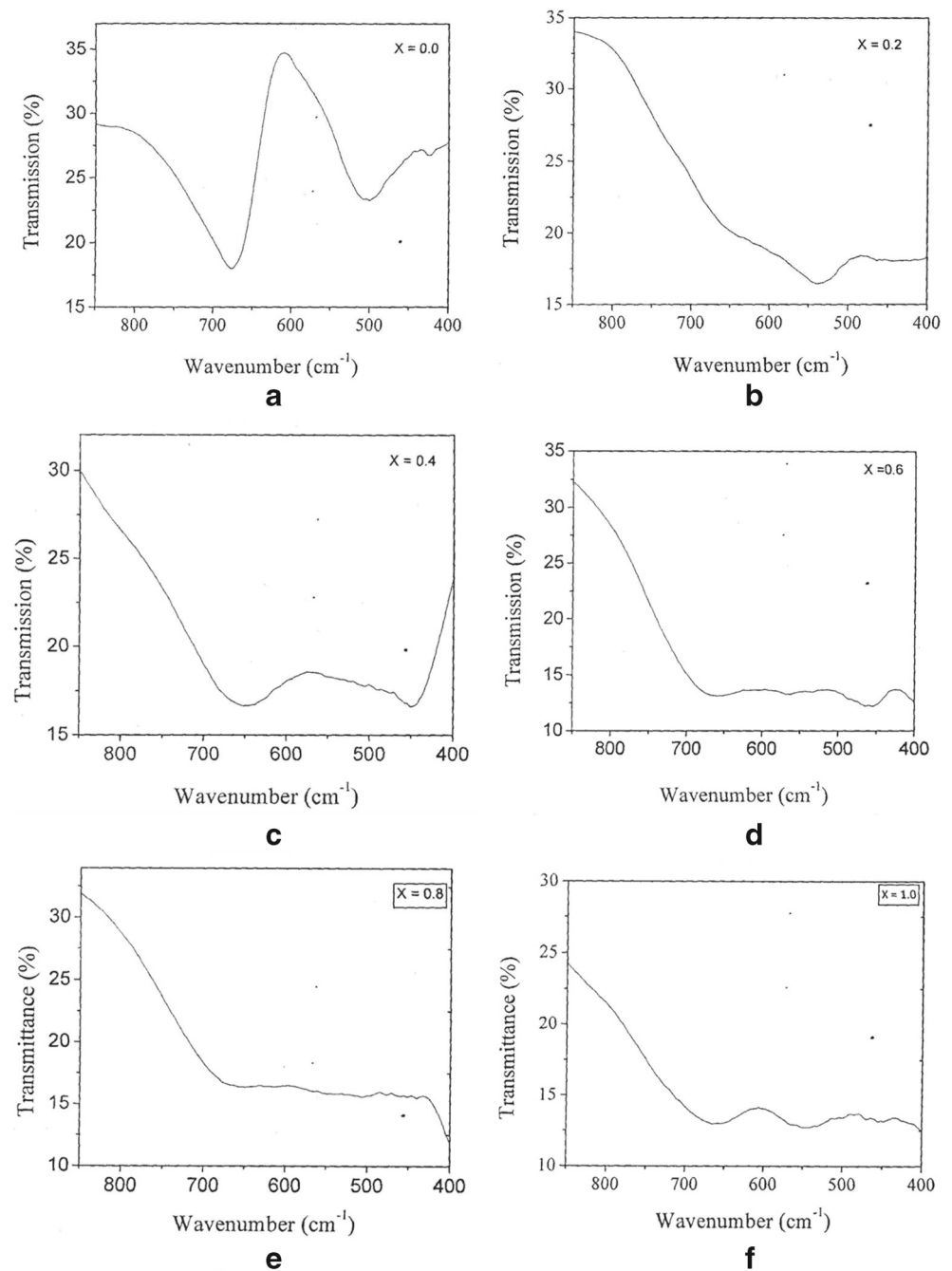


Fig. 6 Variation of iron ratio ($\text{Fe}_A^{3+}/\text{Fe}_B^{3+}$) and ionic radii (r_A and r_B) with composition x of $\text{CoCr}_x\text{Fe}_{2-x}\text{O}_4$ nanoparticles (for $x = 0.0$ to 1.0 in step of 0.2)

Fig. 7 a–f IR-spectra of $\text{CoCr}_x\text{Fe}_{2-x}\text{O}_4$ spinel ferrite nanoparticles (for $x = 0.0$ to 1.0 in step of 0.2)



varies significantly with chromium substitution. The values of bond length R_A and R_B obtained from IR data are given in Table 4.

3.5 Magnetic Properties

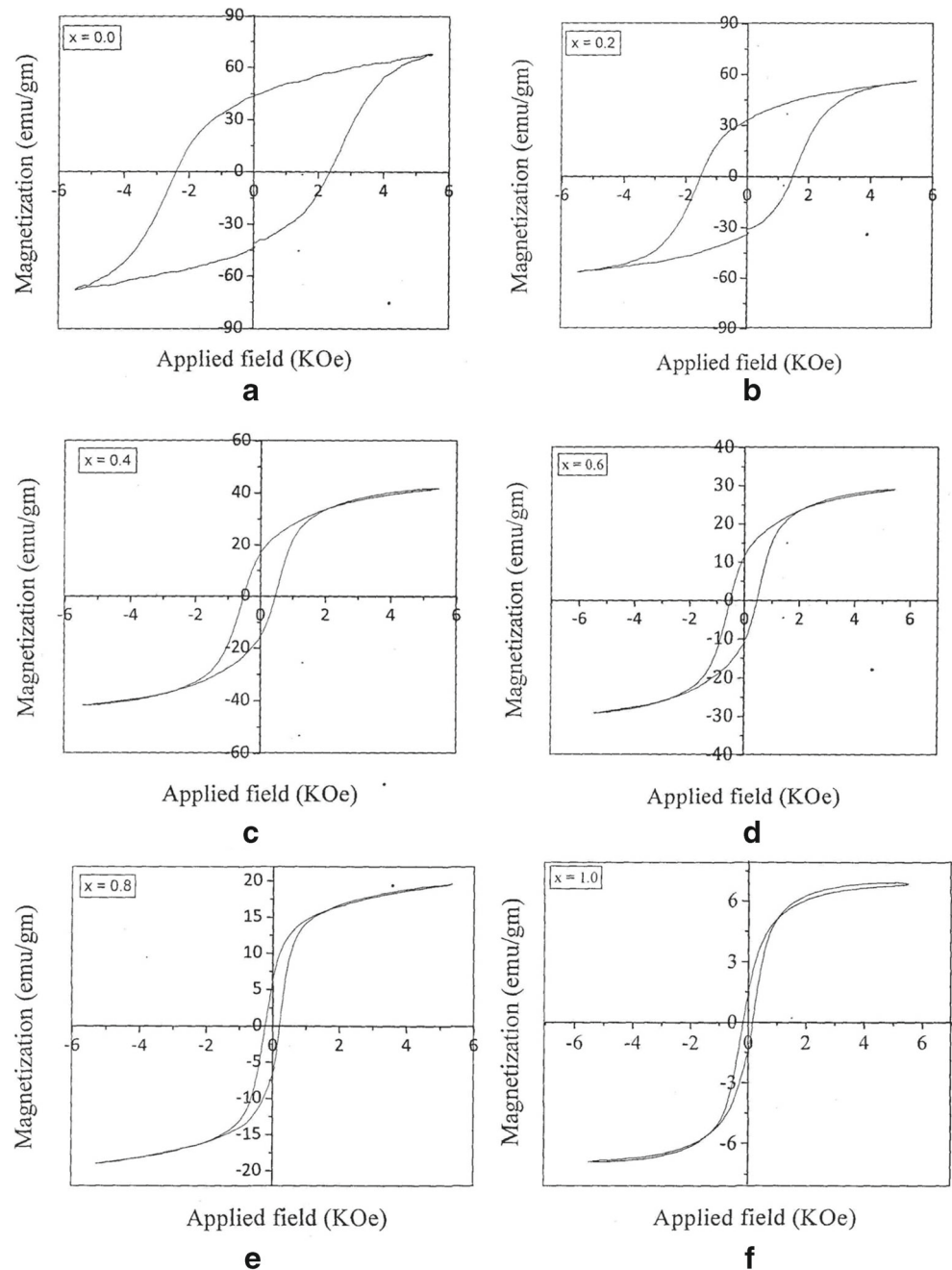
Magnetization measurements for the ferrite system were carried out using the pulse field hysteresis loop technique at 300 K with an applied field of 5 KOe to reach saturation values and the results are plotted as in Fig. 8a–f. Using the

MH plots (Fig. 8a–f) the saturation magnetization (M_S) was obtained for all the samples.

The variation of saturation magnetization with chromium content is shown in Fig. 9. The saturation magnetization decreases with chromium content. The decrease in magnetization is associated with the magnetic interaction between A and B sites. In the present ferrite system Fe^{3+} ions of $5 \mu_B$ magnetic moment are replaced by Cr^{3+} ions of low magnetic moment of $3 \mu_B$. This results in decrease in magnetic moment of octahedral B site and hence the net

Table 4 Band positions (ν_1 and ν_2), force constant (K_O and K_I) and bond length (R_A and R_B) of $\text{CoCr}_x\text{Fe}_{2-x}\text{O}_4$ spinel ferrite nanoparticles

Com. x	Band positions		Force constant		Bond length	
	ν_1 (cm^{-1})	ν_2 (cm^{-1})	$K_O \times 10_5$ (dyne/cm)	$K_I \times 10_5$ (dyne/cm)	R_A	R_B
0.	680	500	1.105	1.760	1.945	0.2440
0.2	660	490	1.116	1.768	1.941	0.2435
0.4	650	448	1.131	1.789	1.938	0.2432
0.6	640	460	1.128	1.775	1.934	0.2426
0.8	635	465	1.179	1.809	1.930	0.2422
1.0	630	469	1.189	1.813	1.924	0.2414

Fig. 8 a–f M - H plots of $\text{CoCr}_x\text{Fe}_{2-x}\text{O}_4$ spinel ferrite nanoparticles (for $x = 0.0$ to 1.0 in step of 0.2)

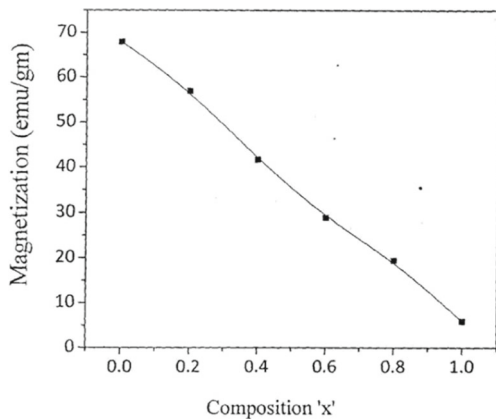


Fig. 9 Variation of magnetization (M_S) with composition x of $\text{CoCr}_x\text{Fe}_{2-x}\text{O}_4$ spinel ferrite nanoparticles (for $x = 0.0$ to 1.0 in step of 0.2)

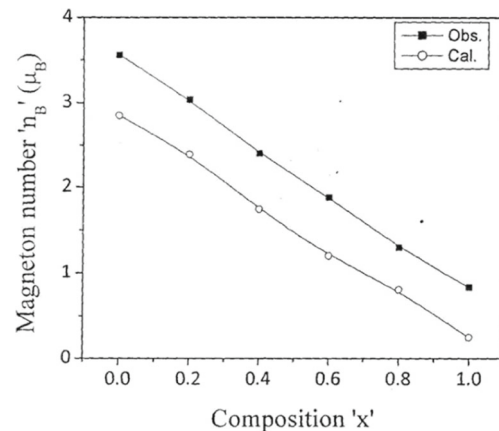


Fig. 10 Variation of observed and calculated magneton number (μ_B) with composition x of $\text{CoCr}_x\text{Fe}_{2-x}\text{O}_4$ spinel ferrite nanoparticles (for $x = 0.0$ to 1.0 in step of 0.2)

magnetic moment of the system decreases with chromium substitution.

According to Neel’s two sub-lattice model of ferri-magnetism, saturation magnetization is given by $M_S = M_B - M_A$ where M_A and M_B are the tetrahedral and octahedral sub-lattice magnetization [38]. The sub-lattice magnetic moment are calculated using the cation distribution data and taking ionic magnetic moment as $3, 3$ and $5 \mu_B$ for Co^{2+} , Cr^{3+} and Fe^{3+} respectively.

The values of Neel’s magnetic moment (calculated magneton number) are given in Table 5. Figure 10 illustrates the variation of observed and calculated magnetic moment as a function of chromium composition x . It is evident from Fig. 10 that both observed and calculated magneton number (n_B) decreases linearly with chromium substitution. The observed and calculated magneton number differs from each other.

The remanence magnetization (M_r) and coercivity (H_C) obtained from MH plots decreases with chromium composition x . The values of M_r and H_C are given in Table 5. The large values of coercivity as can be seen from Table 5 are due to the smaller particle size of the samples. Due to the substitution of chromium ions these magnetic

parameters decreased. The values of M_S , M_r , H_C and R are in the reported range [39].

4 Conclusion

The following conclusions were drawn from the present study:

- The samples of $\text{CoCr}_x\text{Fe}_{2-x}\text{O}_4$ were successfully synthesized by sol-gel auto combustion method.
- Using sol-gel method, the particle size of about 26–38 nm was achieved.
- The lattice parameter decreases with chromium substitution.
- Cation distribution studies revealed that Co^{2+} and Fe^{3+} occupy both A and B sites, whereas Cr^{3+} ions occupy only B site.
- Large values of surface area were observed for present samples.
- Microstructure studied by SEM technique, shows nanosized nature of the samples.
- The broad absorption bands were seen in IR spectra.

Table 5 Magnetization parameters and magneton number (n_B) of $\text{CoCr}_x\text{Fe}_{2-x}\text{O}_4$ spinel ferrite nanoparticles

Com. x	Magnetization parameters				Magneton number n_B (μ_B)	
	M_r (emu/g)	M_S (emu/g)	M_r/M_S	H_C (Oe)	Obs.	Cal.
0.	43.62	67.93	0.64	2329	2.85	3.56
0.2	33.86	57.01	0.59	1480	2.39	3.04
0.4	16.88	41.64	0.41	429	1.74	2.40
0.6	11.5	28.83	0.40	374	1.20	1.88
0.8	4.86	19.46	0.25	197	0.81	1.30
1.0	1.87	5.93	0.32	151	0.25	0.84

- Saturation magnetization, remanence magnetization and coercivity decreases with increase in chromium substitution.
- Observed and calculated magneton number both decreases with chromium substitution.

References

- El Ata, A.A., Attia, S., Meaz, T.: AC Conductivity and dielectric behavior of $\text{CoAl}_x\text{Fe}_{2-x}\text{O}_4$. *Solid State Sci.* **6**, 61–69 (2004)
- Kondo, K., Chiba, T., Yamada, S.: Effect of microstructure on magnetic properties of Ni–Zn ferrites. *J. Magn. Magn. Mater.* **254**, 541–543 (2003)
- Pervaiz, E., Gul, I.: Low temperature synthesis and enhanced electrical properties by substitution of Al_3 and Cr_3 in Co–Ni nanoferrites. *J. Magn. Magn. Mater.* **343**, 194–202 (2013)
- Šafařík, I., Šafaříková, M.: Magnetic Nanoparticles and Biosciences. In: *Nanostructured Materials*, pp. 1–23. Springer (2002)
- Vestal, C.R., Zhang, Z.J.: Effects of surface coordination chemistry on the magnetic properties of MnFe_2O_4 spinel ferrite nanoparticles. *J. Am. Chem. Soc.* **125**, 9828–9833 (2003)
- Song, Q., Zhang, Z.J.: Shape control and associated magnetic properties of spinel cobalt ferrite nanocrystals. *J. Am. Chem. Soc.* **126**, 6164–6168 (2004)
- Chen, Q., Zhang, Z.J.: Size-dependent superparamagnetic properties of MgFe_2O_4 spinel ferrite nanocrystallites. *Appl. Phys. Lett.* **73**, 3156–3158 (1998)
- Kahn, M.L., Zhang, Z.J.: Synthesis and magnetic properties of CoFe_2O_4 spinel ferrite nanoparticles doped with lanthanide ions. *Appl. Phys. Lett.* **78**, 3651–3653 (2001)
- White, R.: Opportunities in magnetic materials. *Science* **229**, 11–15 (1985)
- Yi, D.K., Lee, S.S., Ying, J.Y.: Synthesis and applications of magnetic nanocomposite catalysts. *Chem. Mater.* **18**, 2459–2461 (2006)
- Kale, S.B., Somvanshi, S.B., Sarnaik, M., More, S., Shukla, S., Jadhav, K.: Enhancement in Surface Area and Magnetization of CoFe_2O_4 Nanoparticles for Targeted Drug Delivery Application. In: *AIP Conference Proceedings*, pp. 030193. Publishing (2018)
- Reddy, C.G., Manorama, S., Rao, V.: Semiconducting gas sensor for chlorine based on inverse spinel nickel ferrite, sensors and actuators B. *Chemical* **55**, 90–95 (1999)
- Kharat, P.B., Somvanshi, S.B., Kounsalye, J.S., Deshmukh, S.S., Khirade, P.P., Jadhav, K.: Temperature Dependent Viscosity of Cobalt Ferrite/Ethylene Glycol Ferrofluids. In: *AIP Conference Proceedings*, pp. 050044. Publishing (2018)
- Rondinone, A.J., Liu, C., Zhang, Z.J.: Determination of magnetic anisotropy distribution and anisotropy constant of manganese spinel ferrite nanoparticles. *J. Phys. Chem. B* **105**, 7967–7971 (2001)
- Slonczewski, J.: Anisotropy and magnetostriction in magnetic oxides. *J. Appl. Phys.* **32**, S253–S263 (1961)
- Gul, I., Maqsood, A.: Structural, magnetic and electrical properties of cobalt ferrites prepared by the sol–gel route. *J. Alloys Compd.* **465**, 227–231 (2008)
- Liu, C., Zou, B., Rondinone, A.J., Zhang, Z.J.: Chemical control of superparamagnetic properties of magnesium and cobalt spinel ferrite nanoparticles through atomic level magnetic couplings. *J. Am. Chem. Soc.* **122**, 6263–6267 (2000)
- Zhao, L., Zhang, H., Xing, Y., Song, S., Yu, S., Shi, W., Guo, X., Yang, J., Lei, Y., Cao, F.: Studies on the magnetism of cobalt ferrite nanocrystals synthesized by hydrothermal method. *J. Solid State Chem.* **181**, 245–252 (2008)
- Xiao, S.H., Jiang, W.F., Li, L.Y., Li, X.J.: Low-temperature auto-combustion synthesis and magnetic properties of cobalt ferrite nanopowder. *Mater. Chem. Phys.* **106**, 82–87 (2007)
- Sawatzky, G., Van Der Woude, F., Morrish, A.: Cation distributions in octahedral and tetrahedral sites of the ferrimagnetic spinel CoFe_2O_4 . *J. Appl. Phys.* **39**, 1204–1205 (1968)
- Iqbal, M.J., Siddiquah, M.R.: Electrical and magnetic properties of chromium-substituted cobalt ferrite nanomaterials. *J. Alloys Compd.* **453**, 513–518 (2008)
- Nlebedim, I., Ranvah, N., Williams, P., Melikhov, Y., Snyder, J., Moses, A., Jiles, D.: Effect of heat treatment on the magnetic and magnetoelastic properties of cobalt ferrite. *J. Magn. Magn. Mater.* **322**, 1929–1933 (2010)
- Tahar, L.B., Artus, M., Ammar, S., Smiri, L., Herbst, F., Vaulay, M.-J., Richard, V., Grenèche, J.-M., Villain, F., Fievet, F.: Magnetic properties of $\text{CoFe}_1.9\text{RE}_0.1\text{O}_4$ nanoparticles (RE = La, Ce, Nd, Sm, Eu, Gd, Tb, Ho) prepared in polyol. *J. Magn. Magn. Mater.* **320**, 3242–3250 (2008)
- Nikumbh, A., Pawar, R., Nighot, D., Gugale, G., Sangale, M., Khanvilkar, M., Nagawade, A.: Structural, electrical, magnetic and dielectric properties of rare-earth substituted cobalt ferrites nanoparticles synthesized by the co-precipitation method. *J. Magn. Magn. Mater.* **355**, 201–209 (2014)
- Karimi, Z., Mohammadifar, Y., Shokrollahi, H., Asl, S.K., Yousefi, G., Karimi, L.: Magnetic and structural properties of nano sized Dy-doped cobalt ferrite synthesized by co-precipitation. *J. Magn. Magn. Mater.* **361**, 150–156 (2014)
- Pervaiz, E., Gul, I.: Structural, electrical and magnetic studies of Gd^{3+} doped cobalt ferrite nanoparticles. *Int. J. Current Eng. Technol.* **2**, 377–387 (2012)
- Dascalu, G., Pompilian, G., Chazallon, B., Nica, V., Caltun, O.F., Gurlui, S., Focsa, C.: Rare earth doped cobalt ferrite thin films deposited by PLD. *Appl. Phys. A* **110**, 915–922 (2013)
- Kumar, L., Kar, M.: Effect of La^{3+} substitution on the structural and magnetocrystalline anisotropy of nanocrystalline cobalt ferrite ($\text{CoFe}_{2-x}\text{La}_x\text{O}_4$). *Ceram. Int.* **38**, 4771–4782 (2012)
- Jauhar, S., Singhal, S.: Substituted cobalt nano-ferrites, $\text{CoM}_x\text{Fe}_{2-x}\text{O}_4$ (M = Cr^{3+} , Ni^{2+} , Cu^{2+} , Zn^{2+} ; $0.2x$ 1.0) as heterogeneous catalysts for modified Fenton’s reaction. *Ceram. Int.* **40**, 11845–11855 (2014)
- Panda, R.K., Muduli, R., Jayarao, G., Sanyal, D., Behera, D.: Effect of Cr^{3+} substitution on electric and magnetic properties of cobalt ferrite nanoparticles. *J. Alloys Compd.* **669**, 19–28 (2016)
- Denton, A.R., Ashcroft, N.W.: Vegard’s law. *Phys. Rev. A* **43**, 3161–3164 (1991)
- Lang, L.L., Xu, J., Qi, W.H., Li, Z.Z., Tang, G.D., Shang, Z.F., Zhang, X.Y., Wu, L.Q., Xue, L.C.: Study of cation magnetic moment directions in Cr (Co) doped nickel ferrites. *J. Appl. Phys.* **116**, 123901 (2014)
- Bainade, S.R., Kale, C.M., Sable, M.C.: Effect of Cr^{3+} ions substitution on structural and magnetic properties of co ferrite nanoparticles. *J. Supercond. Novel Magn.* **31**, 387–394 (2018)
- Toksha, B.G., Shirsath, S.E., Mane, M.L., Patange, S.M., Jadhav, S.S., Jadhav, K.M.: Autocombustion high-temperature synthesis, structural, and magnetic properties of $\text{CoCr}_x\text{Fe}_{2-x}\text{O}_4$ ($0 < x < 1.0$). *J. Phys. Chem. C* **115**, 20905–20912 (2011)
- Patange, S.M., Shirsath, S.E., Jangam, G.S., Lohar, K.S., Jadhav, S.S., Jadhav, K.M.: Rietveld structure refinement, cation distribution and magnetic properties of Al^{3+} substituted NiFe_2O_4 nanoparticles. *J. Appl. Phys.* **109**, 053909 (2011)
- Patange, S.M., Shirsath, S.E., Toksha, B.G., Jadhav, S.S., Shukla, S.J., Jadhav, K.M.: Cation distribution by Rietveld, spectral and

- magnetic studies of chromium-substituted nickel ferrites. *Appl. Phys. A* **95**, 429–434 (2009)
37. Baykal, A., Eryiğit, Ş., Sertkol, M., Ünlü, S., Yildiz, A., Shirsath, S.E.: The effect of Cr³⁺ substitution on magnetic properties of CoFe₂O₄ nanoparticles synthesized by microwave combustion route. *J. Supercond. Novel Magn.* **29**, 2395–2400 (2016)
38. Pandit, A.A., Shitre, A.R., Shengule, D.R., Jadhav, K.M.: Magnetic and dielectric properties of Mg_{1+x}Mn_x, Fe_{2-2x}O₄ ferrite system. *J. Mater. Sci.* **40**, 423–428 (2005)
39. Iqbal, M.J., Siddiquah, M.R.: Electrical and magnetic properties of chromium-substituted cobalt ferrite nanomaterials. *J. Alloys Compd.* **453**, 513–518 (2008)